INTERNATIONAL JOURNAL FOR NUMERICAL METHODS IN FLUIDS, VOL. 19, 827–847 (1994)

TVD ALGORITHMS FOR THE SOLUTION OF THE COMPRESSIBLE EULER EQUATIONS ON UNSTRUCTURED MESHES

P. R. M. LYRA AND K. MORGAN

Department of Civil Engineering, University College, Swansea SA2 8PP, U.K.

J. PERAIRE

Department of Aeronautics and Astronautics, MIT, Cambridge, MA 02139, U.S.A.

AND

J. PEIRÓ

Department of Aeronautics, Imperial College, London SW7 2BY, U.K.

SUMMARY

The Galerkin finite element method is used as the basis for the construction of schemes for the solution of the two-dimensional compressible Euler equations on unstructured triangular grids. The use of a side-based data structure readily allows for the construction of a local (structured) stencil and the incorporation of a high-resolution shock-capturing method formulated within the TVD concept. The essential features of the finite element side-based scheme and the 1D TVD approach are described and their numerical implementation is discussed. The choice of limiters and the support for their computation are analysed and the solutions of some inviscid flows, obtained by advancing explicitly in time, are presented.

KEY WORDS TVD Unstructured mesh algorithms Euler equations Hypersonic flows

1. INTRODUCTION

Over the last decade CFD practitioners have devoted much effort to the development and use of unstructured mesh based finite element or finite volume solution procedures for the compressible Euler equations. These efforts have been driven by the promise of rapidly accomplishing the mesh generation for problems involving complex geometries and the inherent flexibility of the approach which readily allows for the incorporation of adaptivity. Significant achievements have been made in the areas of mesh generation, adaptivity and the efficiency of unstructured mesh solution algorithms.[1–3]

The requirement of selectively adding numerical dissipation in the simulation of flows involving strong discontinuities has normally been accomplished within the finite element context by the use of explicit dissipative terms[3] or an FCT scheme.[4] These schemes are computationally efficient but sometimes suffer from a lack of robustness and normally require the adjustment of artificial parameters. In this paper an unstructured grid side-based finite element algorithm is developed.[5] A high-accuracy scheme is obtained by replacing the actual fluxes by consistent numerical fluxes constructed making use of a TVD-like[6,7] artificial viscosity. The resulting

CCC 0271–2091/94/210827–21

Received December 1993
Revised April 1994

scheme is a second-order accurate scheme in the smooth regions of the flow and proves to be oscillation free for the inviscid compressible flows analysed.

The algorithms described in the paper are used to study the motion of an inviscid compressible perfect fluid. Special attention is focused on the influence of the limiter adopted in the TVD formulation on the accuracy of the solution, on the stability of the procedure and, for steady state simulations, on the convergence rate achieved.

2. THE GOVERNING EQUATIONS

The motion of an inviscid compressible non-conducting adiabatic fluid in the absence of external source terms is governed by the Euler equations. This system of equations is considered here in the two-dimensional conservation form

$$\frac{\partial \mathbf{U}}{\partial t} + \frac{\partial \mathbf{F}^j}{\partial x_j} = 0 \quad \text{for } j = 1, 2, \tag{1}$$

where the summation convention is employed and where the vector $\mathbf{U}$ and the inviscid flux vectors $\mathbf{F}^j$ are defined by

$$\mathbf{U} = \begin{bmatrix} \rho \\ \rho u_1 \\ \rho u_2 \\ \rho \varepsilon \end{bmatrix}, \qquad \mathbf{F}^j = \mathbf{F}^j(\mathbf{U}) = \begin{bmatrix} \rho u_j \\ \rho u_1 u_j + p\delta_{1j} \\ \rho u_2 u_j + p\delta_{2j} \\ (\rho \varepsilon + p) u_j \end{bmatrix}. \tag{2}$$

Here ρ denotes the density, p the pressure, ε the total specific energy of the fluid and u_j represents the component of the fluid velocity in the direction x_j of a Cartesian co-ordinate system. The equation set is closed by the addition of the perfect gas equation of state

$$p = (\gamma - 1)\rho(\varepsilon - 0{\cdot}5 u_j u_j), \tag{3}$$

where $\gamma = C_p/C_v$ is the ratio of specific heat coefficients.

The solution of this equation set is sought over a closed spatial domain Ω with boundary surface Γ. The initial/boundary value problem requires additionally boundary and initial conditions, which are taken here in the form

$$\mathbf{F}^n = n^j \mathbf{F}^j = \bar{\mathbf{F}}^n \quad \text{on } \Gamma \text{ for all } t > t_m, \tag{4}$$

$$\mathbf{U}(\mathbf{x}, t_m) = \mathbf{U}_0(\mathbf{x}) \quad \text{for all } \mathbf{x} \text{ in } \Omega \text{ at time } t = t_m, \tag{5}$$

where n^j denotes the component in the direction x_j of the unit outward normal vector to Γ and $\bar{\mathbf{F}}^n$ is the normal flux at the boundary. The exact form of $\bar{\mathbf{F}}^n$ will depend upon the local solution and the boundary being simulated, and $\mathbf{U}_0$ is a known function.

3. SIDE-BASED FINITE ELEMENT METHOD

3.1. Spatial discretization

Following the procedure presented in detail by Peraire *et al.*,[5] the Galerkin finite element approximation for the Euler equation system at node I on a grid of linear triangular elements

leads to an equation which can be expressed in the discrete form

$$\left[\mathbf{M}\frac{d\mathbf{U}}{dt}\right]_I = -\sum_{s=1}^{m_I}\frac{C^j_{II_s}}{2}(\mathbf{F}^j_I + \mathbf{F}^j_{I_s}) + \left\langle \sum_{f=1}^{2} D_f(4\bar{\mathbf{F}}^n_I + 2\bar{\mathbf{F}}^n_{J_f} + \mathbf{F}^n_I - \mathbf{F}^n_{J_f})\right\rangle_I, \tag{6}$$

where m_I is the number of sides in the mesh which are connected to node I and $\mathbf{M}$ represents the consistent finite element mass matrix. In the above expression $C^j_{II_S}$ denotes the weight that must be applied to the average value of the flux in the x_j-direction on the side S, which joins nodes I and I_S, to obtain the contribution made by the side to node I. The weight which is applied to the same quantity to obtain the contribution made by the side S to node I_S will be denoted by $C^j_{I_SI}$. In addition, D_f represents the boundary face correction coefficient which is necessary for nodes I which lie on the boundary, and J_1 and J_2 are the two boundary nodes which are connected to node I. These weights can be readily computed as

$$C^j_{II_S} = -\sum_{E\in II_S}\frac{2\Omega_E}{3}\left[\frac{\partial N_I}{\partial x_j}\right]_E + \left\langle \frac{\Gamma_f}{6}n^j_{II_S}\right\rangle_{II_S} \qquad D_f = \frac{\Gamma_f}{12}, \tag{7}$$

where now the summation extends over the elements that contain the edge II_s and the bracketed term is only non-zero if II_s is a boundary edge. The quantity Γ_f denotes the length of the boundary edge joining nodes I and I_s, and $n^j_{II_s}$ is the component in the x_j-direction of the unit normal to the edge II_s. It is readily verified that these weights satisfy the relations

$$\begin{aligned} &\sum_{s=1}^{m_I} C^j_{II_s} + \left\langle \sum_{f=1}^{2} 6D_f n^j_{II_s}\right\rangle_I = 0 \quad \text{for } j = 1,2 \\ &C^j_{II_s} + C^j_{I_sI} = 0 \quad \text{for } j = 1,2 \text{ and } s = 1,\ldots,m_i. \end{aligned} \tag{8}$$

The corresponding computer code can be written so that equation (6) is formed by looping over each side in the mesh and sending side contributions to the appropriate nodes. The associated data structure consists of the list of nodes I and I_s for each side of the mesh. For notational convenience, we now define the vector $\mathbf{C}_{II_S}$ as

$$\mathbf{C}_{II_s} = (C^1_{II_s}, C^2_{II_s}), \tag{9}$$

with

$$\mathscr{L}_{II_s} = |\mathbf{C}_{II_s}|, \qquad \mathscr{S}^j_{II_s} = C^j_{II_s}|\mathbf{C}_{II_s}| \tag{10}$$

and write equation (6) as

$$\left[\mathbf{M}\frac{d\mathbf{U}}{dt}\right]_I = -\sum_{s=1}^{m_I}\mathscr{L}_{II_s}\frac{\overbrace{(\mathbf{F}^j_I\mathscr{S}^j_{II_s} + \mathbf{F}^j_{I_s}\mathscr{S}^j_{II_s})}^{\mathbf{F}^j_{II_s}}}{2} + \left\langle \sum_{f=1}^{2} D_f(4\bar{\mathbf{F}}^n_I + 2\bar{\mathbf{F}}^n_{J_f} + \mathbf{F}^n_I - \mathbf{F}^n_{J_f})\right\rangle_I. \tag{11}$$

From the asymmetry of the side weights expressed in equation (8), the numerical discretization scheme can be immediately observed to possess a conservation property, in the sense that the sum of the contributions made by any interior side is zero. It is also apparent, using the results of equation (8), that this is a central difference type scheme. To construct practical solution algorithms for the Euler equations, we must therefore replace the actual flux function $\mathbf{F}_{II_s}$ in equation (11) by a consistent numerical flux $\mathscr{F}_{II_s}$. By adopting various forms for this numerical flux function, we are able to construct a number of different algorithms for the solution of the compressible Euler equations.[3,8,9]

This approach can be directly extended to 3D simulations.[3] In addition to being helpful in the derivation of numerical schemes for 2D and 3D analyses, the use of the side-based data structure leads to codes with reduced CPU time and memory requirements when compared with codes which use the traditional element-based data structure.[2,3]

3.2. Time discretization

Equation (11) represents the time evolution of the unknown vector $\mathbf{U}_I(t)$ at node I of the mesh. A practical solution algorithm is produced by further discretizing the time dimension, utilizing an explicit hybrid K stage time-stepping scheme.[10] Assuming that the nodal values $\mathbf{U}_I^m(t)$ are known at time t_m, the solution is advanced over a time step Δt to time t_{m+1} as follows:

$$\begin{aligned}
&\mathbf{U}_I^{(0)} = \mathbf{U}_I^m,\\
&\vdots\\
&\mathbf{U}_I^{(k)} = \mathbf{U}_I^m + \alpha_k \Delta t [\mathbf{M}_L]_I^{-1} \mathbf{R}_I^{(k-1)}, \quad k = 1, \ldots, K,\\
&\vdots\\
&\mathbf{U}_I^{m+1} = \mathbf{U}_I^{(K)},
\end{aligned} \tag{12}$$

where $\mathbf{R}_I^{(k-1)}$ represents the right-hand side of equation (11) at stage k_{-1}. The consistent finite element mass matrix $\mathbf{M}$ has been replaced by the standard lumped (diagonal) mass matrix $\mathbf{M}_L$ in order to enable an explicit time integration. This approximation was adopted for both the transient and steady state computations in the present work.

When a steady state analysis is attempted, a local time stepping[5] is employed to accelerate the convergence rate towards steady state, since the correct modelling of the transient development of the flow is not of interest.

To prevent local spurious negative values of the thermodynamic variables ρ and p during the convergence process, the pressure and density are updated so that they always remain positive,[11] e.g. the pressure is updated according to

$$p^{n+1} = p^n + \Delta p[1 + \eta(\alpha + |\Delta p/p^n|)]^{-1} \tag{13}$$

whenever $\Delta p/p^n \leqslant \alpha$, where $\eta = 2$ and $\alpha = -0{\cdot}2$.

4. ONE-DIMENSIONAL TVD SCHEMES

A practical high-resolution algorithm is produced by adopting the numerical flux for the generalized formulation of the TVD Lax–Wendroff scheme developed by Davis,[12] Roe[13] and Yee,[7] which is written as

$$\mathscr{F}_{II_S} = \tfrac{1}{2}[(\mathbf{F}_I^1 + \mathbf{F}_{I_S}^1) - \mathbf{R}_{II_S} \boldsymbol{\Phi}_{II_S}], \tag{14}$$

with

$$\Phi_{II_S}^l = \lambda^*(\Lambda_{II_S}^l)^2 \hat{Q}_{II_S}^l + |\Lambda_{II_S}^l|(\Delta_{II_S} W^l - \hat{Q}_{II_S}^l), \tag{15}$$

where $\lambda^* = \Delta t/\Delta L$, with ΔL being the side length and Δt the local time step. The superscript l denotes the lth characteristic field and

$$\Delta_{II_S} \mathbf{W} = \mathbf{R}_{II_S}^{-1} \Delta_{II_S} \mathbf{U}. \tag{16}$$

Here $\mathbf{R}$ and $\mathbf{R}^{-1}$ denote the matrices whose columns are the right and left eigenvectors of the

Figure 1. One-dimensional stencil

Jacobian matrix $\mathbf{A}^l$ respectively, $\Lambda^l_{II_S}$ is the lth eigenvalue of $\mathbf{A}^l$ and the parameter $\hat{Q}^l_{II_S}$. represents the limiter which is computed in terms of the gradients of the characteristic variables $\Delta_{II_S}W^l$. The Jacobian matrix $\mathbf{A}^l$ is computed using Roe's average[14] between the two states $\mathbf{U}_I$ and $\mathbf{U}_{I_S}$, and Harten's[15] entropy correction is used to eliminate non-physical solutions.

Since the introduction of the notation of TVD schemes by Harten,[6] necessary and sufficient conditions have been generalized for non-linear difference schemes to be TVD. The interested reader is referred to the available literature on this subject.[15–17]

The main mechanism for ensuring a higher-order TVD scheme is the use of non-linear limiters. The limiters impose constraints on the gradients of either the dependent variable (slope limiters) or the flux function (flux limiters). Sweby[16] gives detailed conditions on the limiter function in order to satisfy sufficient TVD conditions. Some of the commonly used limiter functions $\hat{Q}^l_{II_S}$ will be studied in this work. In the definitions that follow, a four-point stencil I_L, I, I_S, I_R is considered (see Figure 1).

Upwind limiters

The limiter function $\hat{Q}^l_{II_S}$ expressed in terms of the characteristic variables can be computed with two parameters as arguments in typical upwind-biased stencils, i.e. it depends on the direction of the flow locally. For $\Lambda^l_{II_S} > 0$ typical upwind limiters are as follows.

(UL.1) Minimod limiter

$$\hat{Q}^l_{II_S} = minmod[\Delta_{II_S}W^l, \beta\Delta_{I_LI}W^l], \tag{17}$$

where β represents a parameter that makes the limiter more compressive and $1 \leqslant \beta \leqslant 2$ for fully explicit schemes. The function '*minmod*' is defined according to

$$minmod[a, \beta b] = \text{sign}(a)\ \max[0, \min(|a|, \beta b\ \text{sign}(a))]. \tag{18}$$

(UL.2) Woodward–Colella limiter[18]

$$\hat{Q}^l_{II_S} = minmod[2\Delta_{I_LI}W^l, 2\Delta_{II_S}W^l, \tfrac{1}{2}(\Delta_{I_LI}W^l + \Delta_{II_S}W^l)]. \tag{19}$$

(UL.3) Roe superbee limiter[13]

$$\hat{Q}^l_{II_S} = \text{supb}[\Delta_{I_LI}W^l, \Delta_{II_S}W^l]. \tag{20}$$

where 'supb' is the function defined by

$$\text{supb}[a, b] = \text{sign}(a)\ \max[0, \min(2|a|, b\ \text{sign}(a)), \min(|a|, 2b\ \text{sign}(a))]. \tag{21}$$

(UL.4) Van Albada limiter[19]

$$\hat{Q}^l_{II_S} = \frac{\Delta_{I_LI} W^l(\Delta^2_{II_S} W^l + \delta_2) + \Delta_{II_S} W^l(\Delta^2_{I_LI} W^l + \delta_2)}{\Delta^2_{II_S} W^l + \Delta^2_{I_LI} W^l + 2\delta_2}, \tag{22}$$

where δ_2 is a small parameter to prevent the appearance of a zero in the denominator.

Symmetric limiters

The limiter function $\hat{Q}^l_{II_S}$ can also be computed with three parameters as arguments in a typical symmetric stencil.

For instance, the function '*minmod*' can be redefined as a three-argument function similar to expression (18), where it returns the value zero if any of its arguments are of opposite sign and returns the smallest argument in absolute value if the arguments are all of the same sign. In this case the '*minmod*' limiter is given by

$$\hat{Q}^l_{II_S} = minmod[\beta\Delta_{I_LI} W^l,\ \Delta_{II_S} W^l,\ \beta\Delta_{I_SI_R} W^l]. \tag{23}$$

Performing the same procedure for the previously defined upwind limiters (UL.1)–(UL.4), we get the corresponding symmetric limiters referred to in this paper as (SL.1)–(SL.4). An alternative way to obtain symmetric limiters is to redefine these limiters as separable functions, given in a general form as

$$\hat{Q}^l_{II_S} = \Theta[\Delta_{I_LI} W^l,\ \Delta_{II_S} W^l] + \Theta[\Delta_{II_S} W^l,\ \Delta_{II_R} W^l] - \Delta_{II_S} W^l, \tag{24}$$

where Θ, a function of either an upwind- or a downwind-biased stencil, can be any of the upwind limiters described above. The separable limiters may give negative values with changes in slope directions, thus failing to satisfy one of the TVD necessary conditions ($\hat{Q}^l_{II_S} \geqslant 0$), and non-monotonic behaviour can result.

5. MULTIDIMENSIONAL TVD EXTENSION

At present, truly multidimensional upwind schemes for the compressible Euler equations are still in the research stage of development. The available theory is complicated and the implementation for practical applications is currently expensive. Here we follow the alternative approach of using the side-based data structure described in Section 3 to build a scheme by employing the 1D TVD concepts in the direction of each side. In this way the numerical flux given by equations (14)–(16) is directly extended to give a two-dimensional counterpart. For example, the numerical flux

$$\mathscr{F}_{II_S} = \tfrac{1}{2}\{(\mathbf{F}^j_I \mathscr{S}^j_{II_S} + \mathbf{F}^j_{I_S} \mathscr{S}^j_{II_S}) - \mathbf{R}_{II_S}[\lambda^*(\Lambda_{II_S})^2 \hat{Q}_{II_S} + |\Lambda_{II_S}|(\Delta_{II_S}\mathbf{W} - \hat{\mathbf{Q}}_{II_S})]\} \tag{25}$$

represents the extension of the 1D Lax–Wendroff TVD (LW/TVD) scheme to unstructured meshes. The resulting scheme is referred to here as a symmetric TVD scheme, since the upwinding is introduced only in the presence of the limiter and in the direction in which the second-order inviscid fluxes propagate, e.g. in the direction of the weight coefficients $\mathbf{C}_{II_S}$.

A limiting procedure can be obtained by introducing ghost (or dummy) nodes as described in Figure 2. For edge S the ghost nodes I_L and I_R are located equidistantly along the line which contains the nodes I and I_S. To evaluate the state variables at ghost nodes, a direct linear

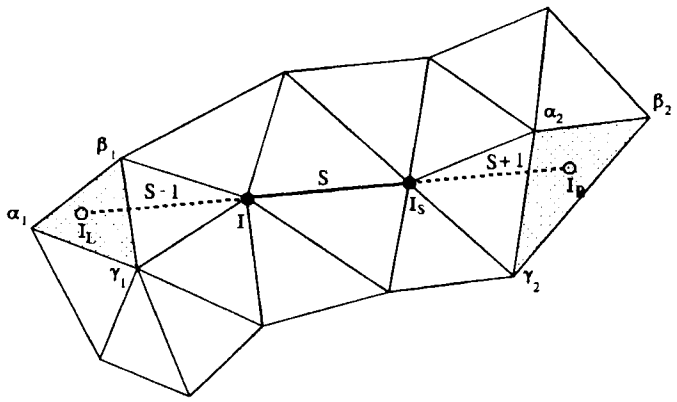

Figure 2. Location of ghost nodes in a generic triangular grid

interpolation employing the element shape functions is used. When a dummy node falls outside the computational domain, either a constant (locally first-order scheme) or a linear extrapolation (locally second-order scheme) can be adopted. The limiter $\hat{Q}'_{II_S}$ is then computed as for the 1D system of equations by making use of the 'local structured' stencil which has been built for each side of the mesh.

The three nodes of the triangle that contains the ghost node, and the two shape functions evaluated at the ghost node for the interpolation step, are kept in memory for each of the two ghost nodes that belong to each side. This procedure represents a memory overhead of 10 times the local number of sides in a 2D computation. In the numerical steady state applications presented in this paper we have dropped the Lax–Wendroff term as suggested by Yee[7] from the numerical flux described in equation (25), i.e. λ^* is set equal to zero. The resultant Galerkin TVD (G/TVD) scheme can be considered as a rational way to introduce artificial dissipation which is suitable for separate space and time discretizations.

6. NUMERICAL APPLICATIONS

The triangulation adopted for the 2D computations was obtained by making use of the advancing front technique due to Peraire *et al.*[20] An adaptive mesh enrichment procedure for steady state solution was used to improve the accuracy of the presented computations. For this procedure the error indicator is side-based and results in the introduction of new nodes for each side for which the calculated error exceeds a certain proportion of the maximum error. Further details about the error analysis involved in the procedure and about the adaptive procedure itself can be found in Reference 2. Unless it is specifically mentioned to the contrary, a Galerkin TVD scheme with one-stage explicit time integration is adopted in the following examples.

6.1 Shock tube problem

The shock tube problem[21] constitutes a particularly interesting and difficult test case for validation of algorithms to solve the full 1D Euler equation set. In addition, it allows insight to the strengths and weaknesses of the scheme when different limiters are adopted. A schematic description of the flow behaviour is presented in Figure 3, where the typical solution to the

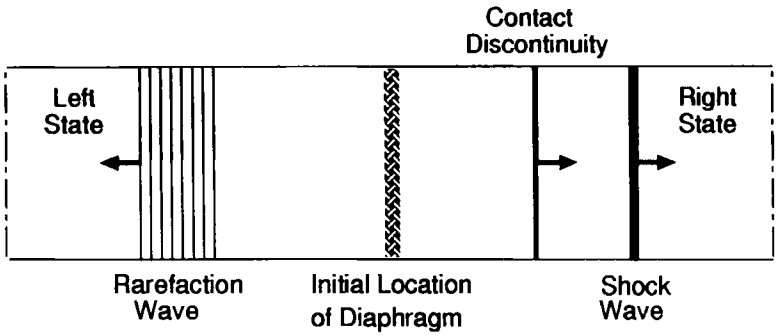

Figure 3. Typical solution to the Riemann problem for the Euler equations

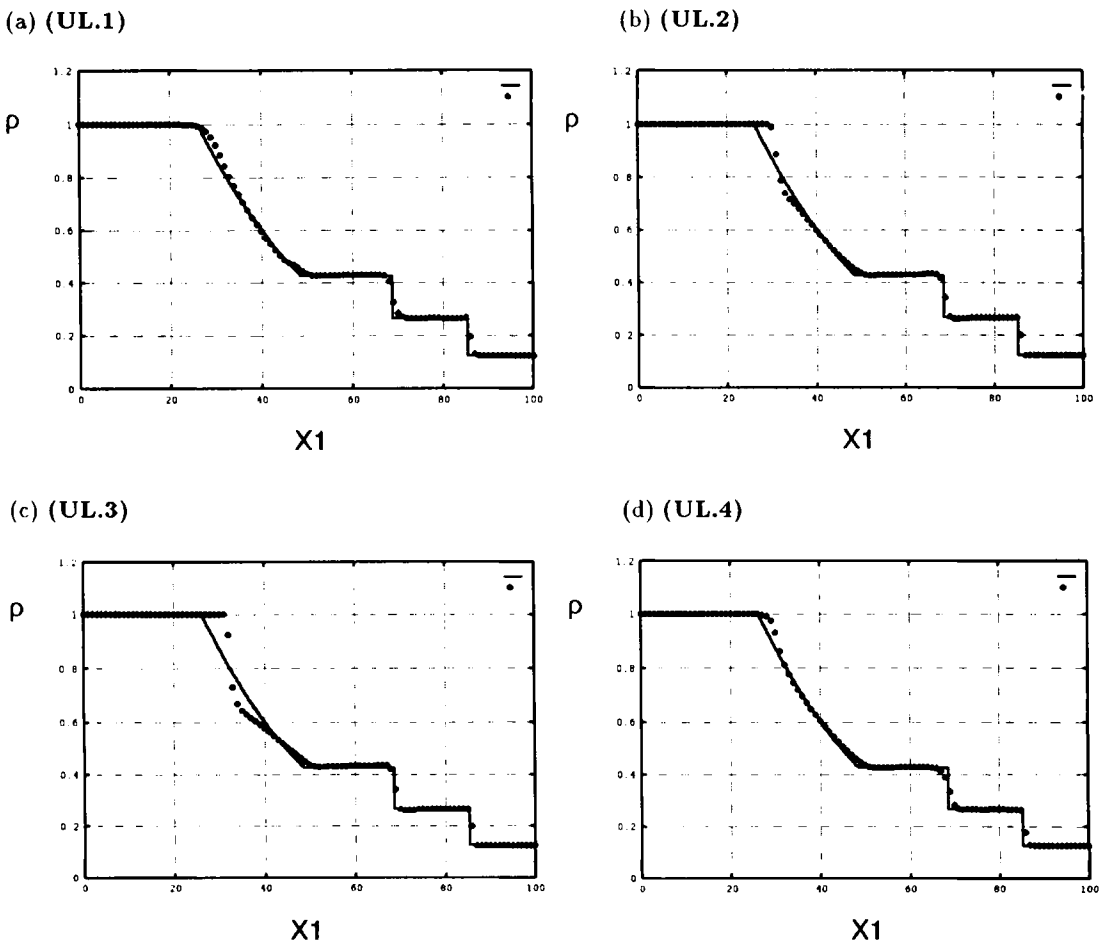

Figure 4. Shock tube problem: computed density by the G/TVD scheme with limiters computed in an upwind-biased stencil

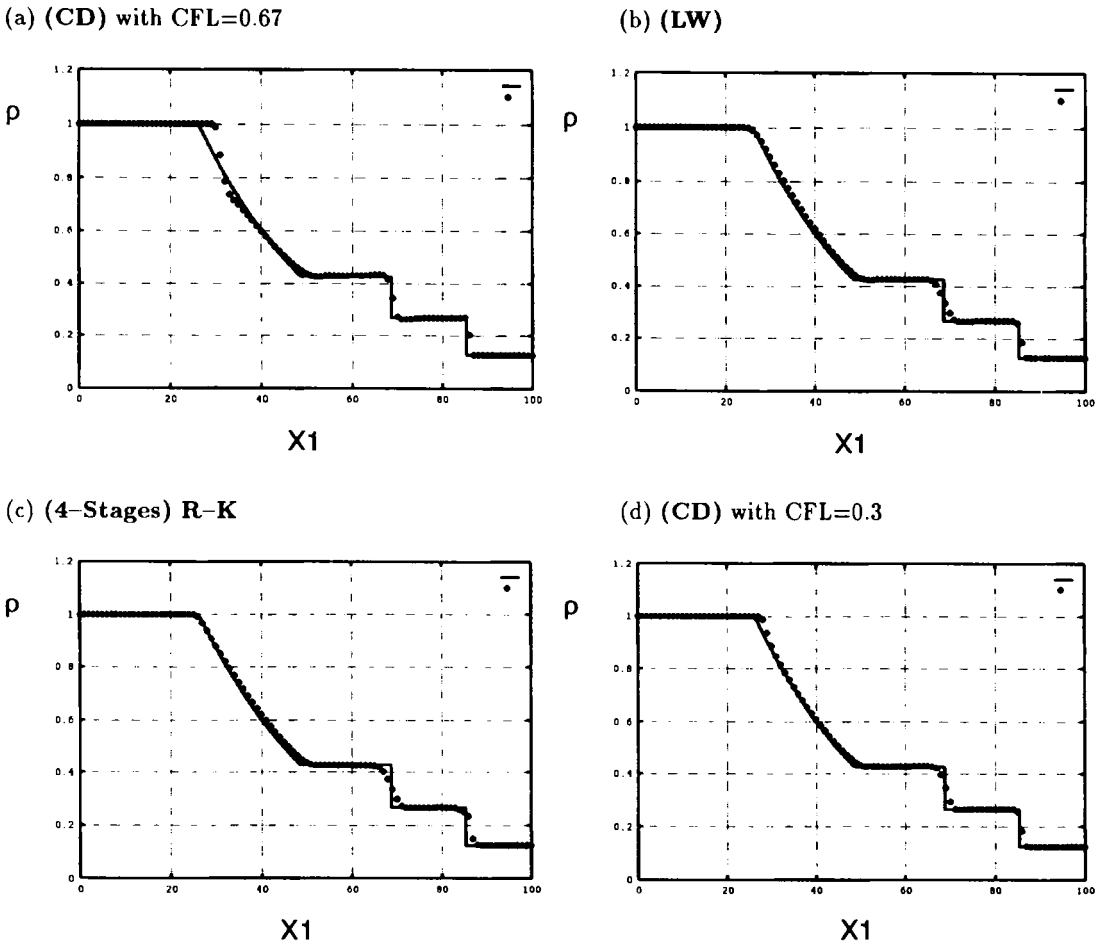

Figure 5. Shock tube problem: computed density by a TVD scheme with the Woodward–Colella limiter (UL.2) computed in an upwind-biased stencil

problem has a contact discontinuity and two non-linear waves, each of which might be either a shock or a rarefaction wave depending on the left and right states. A moderate shock pressure ratio of 2·031 is chosen and the initial condition consists of two semi-infinite states separated at time $t = 0$. The left and right states are set to the following conditions:

$$\begin{bmatrix} \rho_L \\ u_L \\ p_L \end{bmatrix} = \begin{bmatrix} 1{\cdot}0 \\ 0{\cdot}0 \\ 1{\cdot}0 \end{bmatrix} \quad \text{for } x_1 \leqslant 50{\cdot}0, \qquad \begin{bmatrix} \rho_R \\ u_R \\ p_R \end{bmatrix} = \begin{bmatrix} 0{\cdot}125 \\ 0{\cdot}0 \\ 0{\cdot}1 \end{bmatrix} \quad \text{for } x_1 > 50{\cdot}0. \tag{26}$$

In the following analysis we use a CFL number of $\frac{2}{3}$. The number of discrete points in the mesh is 101. The time for stopping the computation ($t = 20{\cdot}0$) has been chosen in order to use the full computational domain and corresponds to 66 time steps. In Figure 4 the use of the upwind limiters (UL.1)–(UL.4) is analysed. With the '*minmod*' limiter a compressive parameter $\beta = 2{\cdot}0$ was used. All the limiters prove to be accurate in capturing the shock and contact

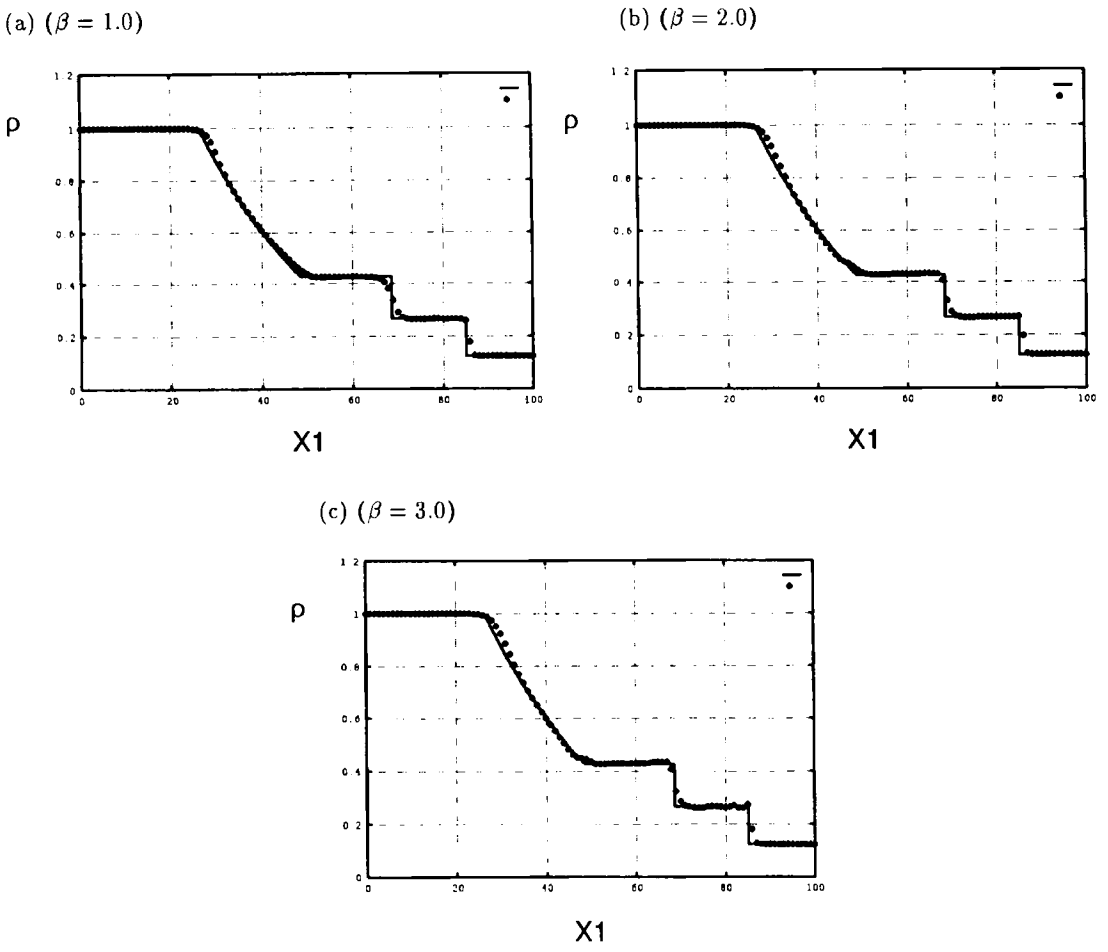

Figure 6. Shock tube problem: study of the effect of the compressive parameter β when the '*minmod*' limiter (UL.1) computed in an upwind-biased stencil is adopted

discontinuity with roughly one to two transition points. However, their behaviour for the smooth portion of the solution cannot be adequate since they are overcompressive, i.e. the gradients of flow variables are made steeper with the formation of a non-physical expansion shock, which is clearly apparent when the Roe 'superbee' (UL.3) and Woodward–Colella (UL.2) limiters are considered.

The remedy for this problem can be the use of the full Lax–Wendroff TVD numerical flux, the adoption of multistage time integration or a reduction in the CFL number. This is illustrated in Figure 5, where the Woodward–Colella (UL.2) limiter is studied. The elimination of the non-physical expansion shock was achieved at the expense of spreading the contact discontinuity and increasing the computational time to reach the same time level.

The adoption of a compressive factor $\beta > 1{\cdot}0$ proves to be very important to enhance the precision of the contact discontinuity simulated with the '*minmod*' limiter (see Figure 6). However, the use of values for β above the upper limit $\beta = 2$ leads to a non-linear instability with oscillations emerging near the shock, as predicted theoretically.

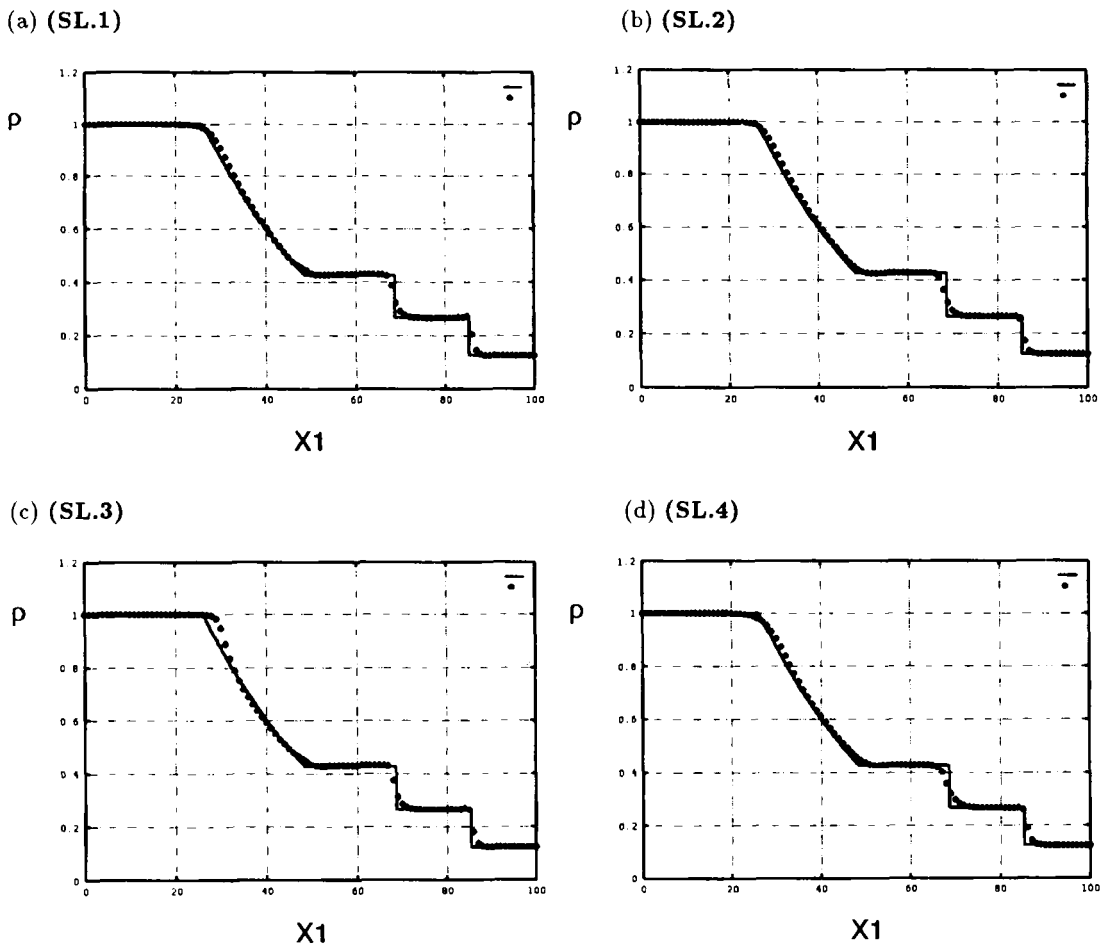

Figure 7. Shock tube problem: computed density by the G/TVD scheme with limiters computed in an symmetric stencil

The adoption of symmetric limiters always provides lower resolution, mainly on the contact discontinuity, as can be seen when the results presented in Figure 7 are compared with those shown in Figure 4. However, apart from the 'superbee' limiter (SL.3), where an expansion shock appears on the upper portion of the expansion fan, no physically meaningless results or stability problems are present. The separable symmetric limiters as described in equation (24) have more restrictive CFL conditions. For example, the use of Θ equal to 'minimod' needs a reduction in the CFL number to $\frac{4}{7}$ in order to make it stable. The results in general are similar to those obtained with the use of the corresponding non-separable limiters and therefore the non-separable limiters should be preferred.

In the local characteristic, approach, a scalar scheme is applied to each characteristic field. This adds the flexibility of adopting different limiters and even different supports for the computation for each different field. Yee[17] suggests that for problems containing contact discontinuities as well as shocks, mixing the limiters, i.e. using different limiters for each characteristic field, can improve the overall performance of the scheme. A more compressive limiter should be adopted for the linear fields in order to enhance the contact discontinuities,

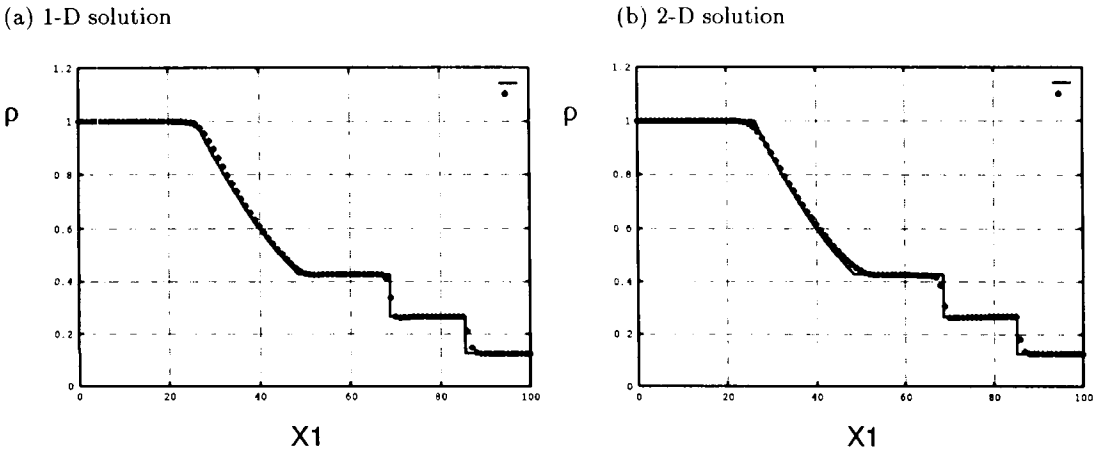

Figure 8. Shock tube problem: G/TVD simulations using mixed limiters ((UL.3), (SL.2), (SL.2))

while for the non-linear fields more robust limiters might be used in order to get better stability and convergence behaviour. In Figure 8(a) we present a result obtained by mixing the limiters in this fashion. All flow features are noticeably well resolved, with very sharp capture of discontinuities and excellent representation of the smooth portion of the solution.

A 2D simulation of this 1D problem was performed with the same mixture of limiters on the computational mesh shown in Figure 9. The results in terms of the density distribution can be seen in Figure 8(b), where it can be observed that the corner of the expansion fan is slightly more rounded for the 2D results. Apart from this, the results are very similar, demonstrating the good performance of the proposed unstructured high-resolution algorithm for this problem. It was also observed that the adoption of linear extrapolation for the values at the dummy nodes that fall outside the domain leads to some oscillations. For this reason the solution was obtained by making use of a constant extrapolation, e.g. the first-order upwind scheme is used for the contribution of the 'dummy side' connecting the actual node to the dummy node in this case.

The adoption of any of the limiters studied gives reasonable results if an appropriate CFL value is chosen, but the differences in accuracy, stability and convergence behaviour indicate that careful consideration must be given to the choice of the limiter. This is expected to be crucial when the code is extended to deal with viscous analysis. It is important to mention that only the Van Albada limiter of the limiters presented here is differentiable and this property can be important when time-accurate implicit TVD schemes are used.[22] Similar studies to these have also been made recently by Rider[23] and Scott and Niu.[24]

6.2. Oblique shock on a flat plate

In the second example, a problem of regular shock reflection at a flat plate is investigated. A flow impinging on the plate at a Mach number of 2·0 and at an angle of attack of $-10°$ is considered. A regular triangular mesh is used to discretize a square domain with 1800 elements

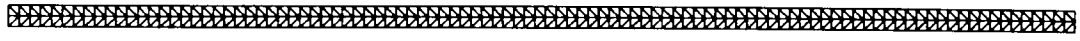

Figure 9. Mesh used for 2D simulation of the shock tube problem

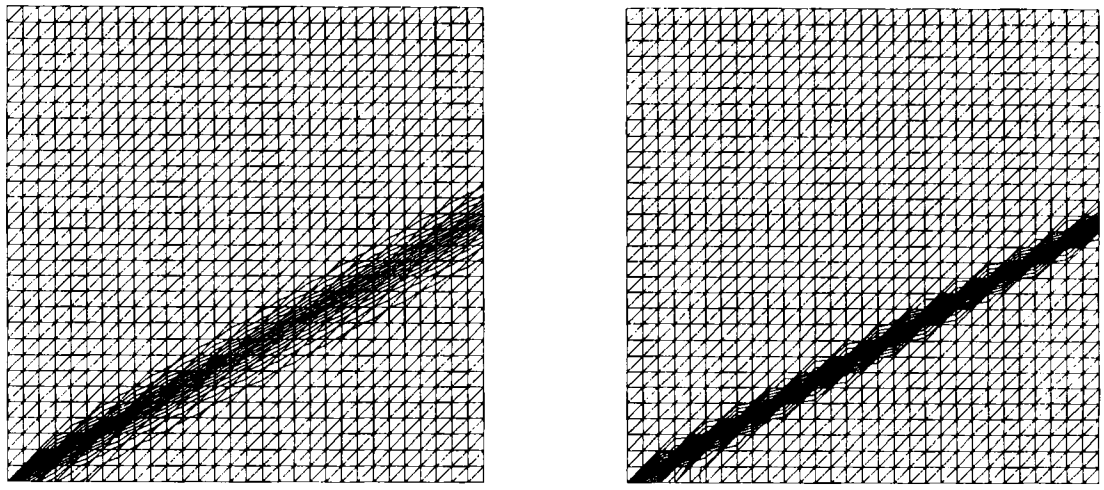

(a) (b)

Figure 10. Oblique shock on a flat plate at Mach 2: computed density contours using (a) the first-order upwind scheme and (b) the G/TVD scheme

and 961 nodes and the value of 0·5 for the CFL number is adopted. The density contours together with the mesh for both an upwind first-order scheme and the Galerkin TVD scheme with limiter (UL.2) are shown in Figure 10. This simple test case allows an insight into the performance of the high-resolution scheme proposed for two-dimensional simulations.

It can be observed that no undershoot or overshoot appears in either solution. However, the improvement in shock resolution of the quasi-second-order TVD scheme is obvious from the figures. No mixing of limiters was attempted, since only a shock is present in the solution. An idea of the high resolution achieved over the first-order scheme can also be seen in Figure 11, where basically only one intermediate node is seen to be necessary to represent the discontinuity.

Figure 12 shows the total variation for the characteristic variables during the time evolution. It can be observed that even with the use of a local time stepping, the total variation does not grow after the impulsive start from the freestream condition. This suggests that the transient solution is also free from spurious oscillations.

The convergence histories of the L_2-norm of the density residual R_ρ for the computations described above and also for the computations with LW/TVD with limiter (UL.2) and G/TVD with limiter (SL.1) with $\beta = 1{\cdot}0$ are presented in Figure 13(a), where a logarithmic scaling on the Y-axis is adopted. The observed behaviour of the G/TVD algorithm is believed to be due to the lack of background dissipation when the second-order Lax–Wendroff term is dropped from the numerical flux and/or the non-linear nature of the limiting procedure. It seems that the limiter reacts to small-scale oscillations in smooth regions and thus introduces too much non-linearity. Some researchers suggest that freezing the limiter when the solution approaches steady state helps to drop the residual towards machine zero. The convergence history with freezing of the limiters after the L_2-norm of the residual of the conservative variables drops by three orders of magnitude for the G/TVD scheme with limiter (UL.2) can be observed in Figure 13(b), where the convergence rate returns to its initial form. It must be mentioned that at this

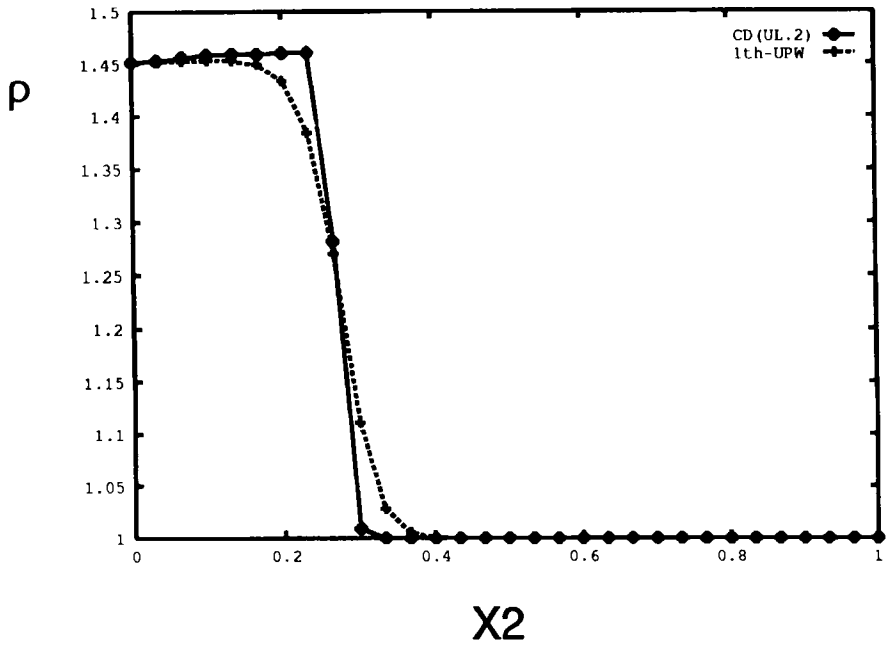

Figure 11. Computed density at $x_1 = 0{\cdot}5$ for the oblique shock on a flat plate at Mach 2

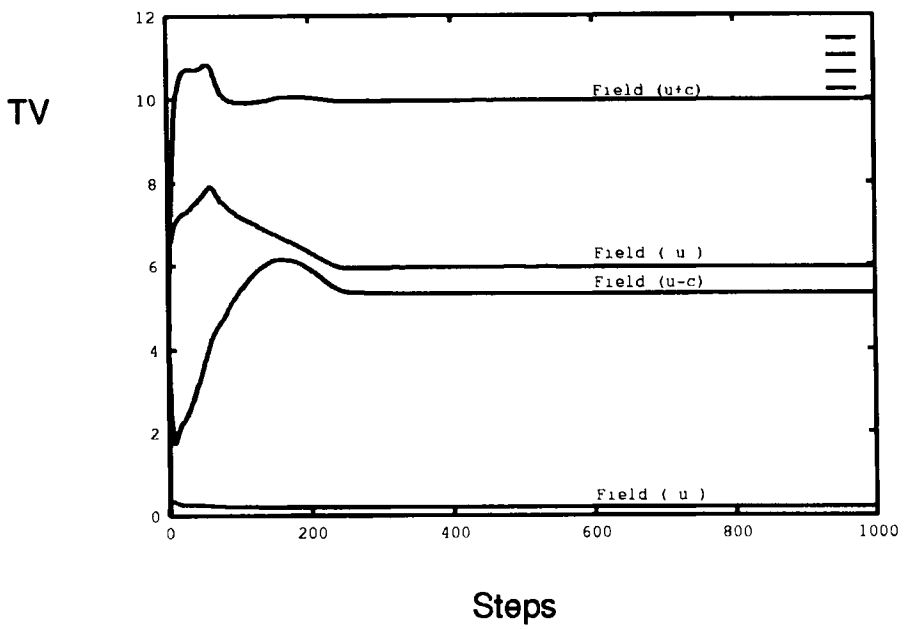

Figure 12. Total variation of the characteristic variables for the G/TVD discrete solution of the oblique shock on a flat plate

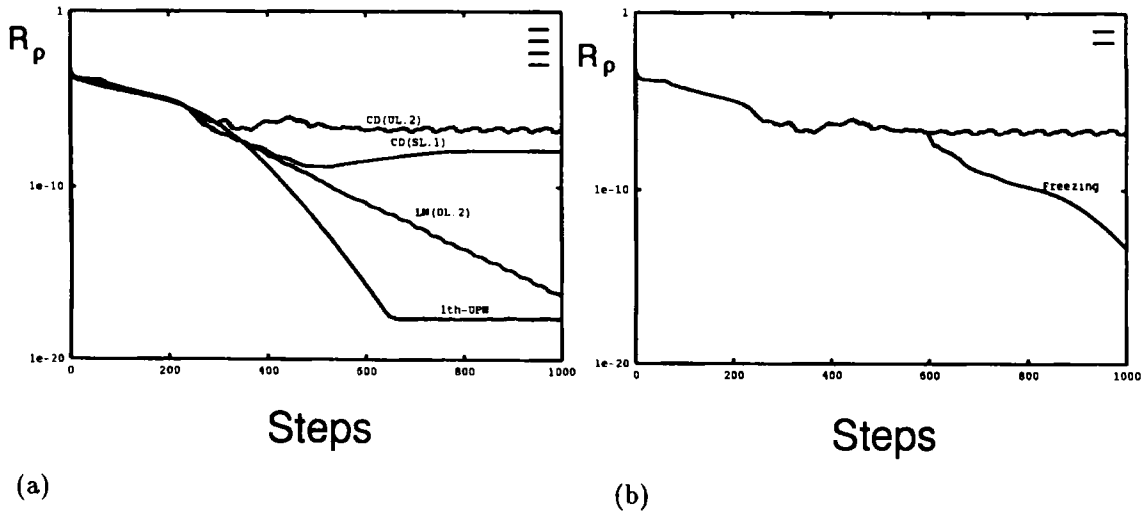

Figure 13. Convergence history of the L_2-norm of the density residuals for the oblique shock on a flat plate: (a) different schemes; (b) the G/TVD scheme with limiter (UL.2)

stage the total variation was already constant, the solution was already approaching steady state and no considerable difference was found in the solution with the adoption of the freezing strategy.

6.3. *Flow past a cylinder*

The third example consists of a steady flow past a circular cylinder at a freestream Mach number of 3·0. A '*minmod*' symmetric limiter (SL.1) with $\beta = 1{\cdot}0$ was adopted. The presence of sonic, stagnation and rarefaction zones makes this problem quite challenging in terms of stability behaviour. The entropy parameter δ_1 was found to exert an important role. For the first mesh analysed (not shown here) the adoption of a very small value for δ_1 resulted in bad convergence behaviour. For example, the L_2-norm of the density residual dropped by only two orders of magnitude after 10,000 steps for $\delta_1 = 0{\cdot}02$, while it dropped by six orders for the same number of steps when δ_1 was increased to 0·1. No freezing of limiters was used here. In terms of the solution obtained, the only difference observed with the use of different values of δ_1 was in the circulation zone behind the cylinder. The final mesh, following one adaptation, and the corresponding Mach number contours are shown in Figure 14. The mesh consists of 24,979 elements and 12,651 nodes. Note that both the bow shock and the quasi-rarefaction zone behind the cylinder are well represented, with the circulation and the weak shocks also being captured.

The variations in the computed Mach number and pressure coefficient along the symmetry line and over the cylinder are presented in Figure 15, where the sharp capture of discontinuities is apparent despite the use of a rather diffusive limiter. In Figure 15(a) we can observe the Mach number drop through the bow shock ahead of the circular cylinder, the acceleration over the cylinder followed by another drop at the back where it goes to zero, the circulation behind the cylinder and an increase downstream indicating the end of the subsonic region. The corresponding pressure coefficient distribution, with similar features, can be seen in Figure 15(b). The reduction in pressure to values close to zero at the back of the cylinder leads to negative values

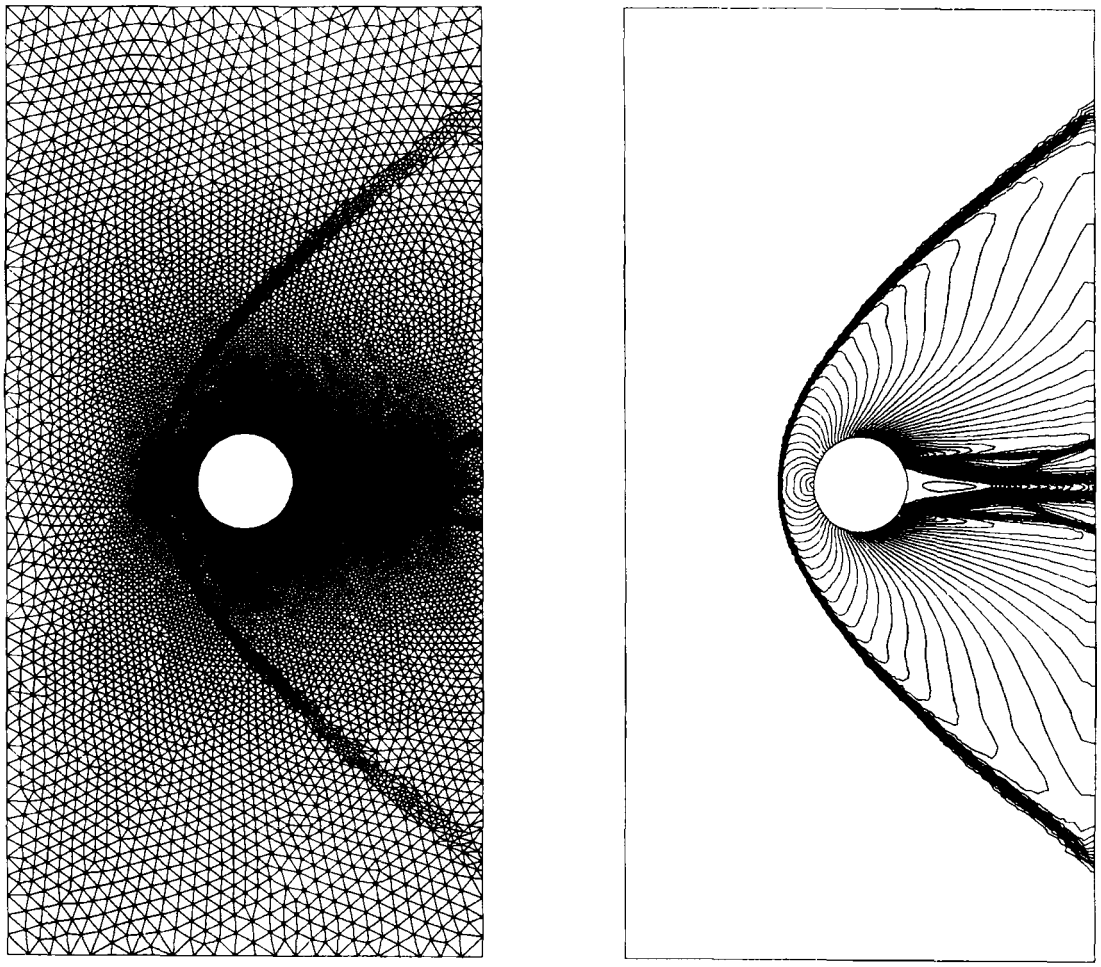

(a) (b)

Figure 14. Steady flow past a cylinder at Mach 3: (a) final mesh; (b) corresponding computed distribution of Mach number contours

at the beginning of the time integration. The procedure described in equation (13) was automatically activated to prevent this from occurring.

6.4. Shock interaction on a cylinder

The previous examples involve computations in a relatively low supersonic regime. The computation of an impinging shock interacting with the bow shock ahead of a circular cylinder at high hypersonic Mach number is the final example considered. The computation starts with the appropriate freestream and oblique shock boundary conditions. Here the undisturbed free Mach number is 15·0 and the disturbed flow has a Mach number of 10·596 with 6° angle of attack. This is an application with practical interest to the design of hypersonic vehicles,[2] since

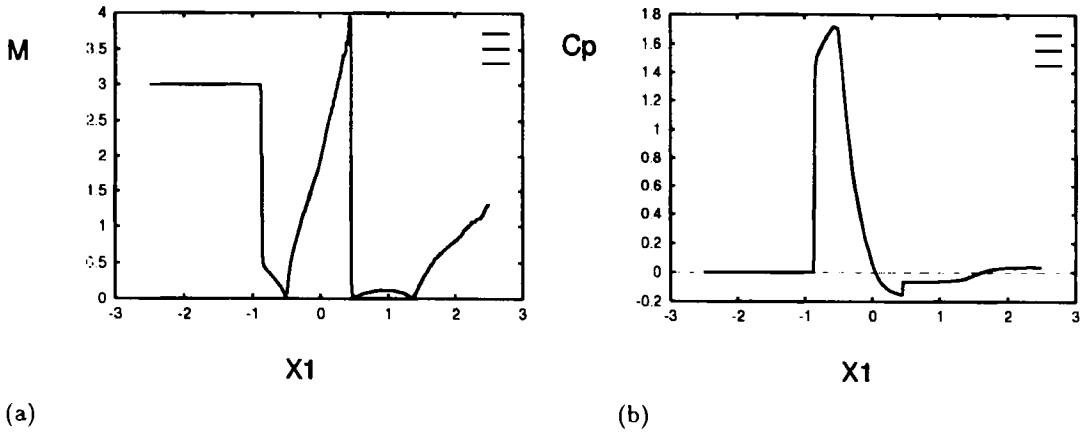

(a) (b)

Figure 15. Steady flow past a cylinder at Mach 3: (a) computed Mach number; (b) computed pressure coefficient on centre-line and cylinder surface

the flow field is typical of that which may be experienced by the inlet cowl of such a vehicle. The values CFL = 0·4, $\delta_1 = 0{\cdot}1$ and the symmetric limiter (SL.1) with $\beta = 1{\cdot}0$ were adopted. This choice is justified by the robustness of the simple '*minmod*' limiter, which gives good stability behaviour, and by the fact that the intermediate solutions in the adaptive procedure only drive the procedure and do not need to be very accurate. The initial and fifth meshes analysed with respectively 3217 and 14,693 elements are shown in Figure 16. The corresponding Mach number contours are presented in Figure 17.

It should be noted that even with a very coarse mesh the Galerkin TVD procedure resolves the main shock within two elements. The staircase phenomenon is due to the relative direction between mesh and shock, and in order to properly resolve the interaction region in front of the cylinder, a finer mesh is needed. Adaptive mesh refinement appears to be the best choice for the location of new nodes in the domain in order to enhance the solution accuracy. Although the pattern of the flow is significantly more complex than in the previous applications, the convergence rate remains quite satisfactory. The mesh adaptivity was performed, using the density and velocity fields for the computation of the error indicator, after the L_2-norm of the density residual drops by five orders of magnitude on each mesh. This was achieved after approximately 10,000 steps. The mesh enrichment proves to be extremely important in enhancing the resolution of the bow shock and also in allowing the capture of the shock-on-shock interaction on the front part of the cylinder.

The variations in pressure over the cylinder on the initial mesh computed using the quasi-second-order TVD scheme with limiters (SL.1) and (SL.4) are plotted together with the first-order upwind solution in Figure 18(a). The solutions on the final mesh using the first-order upwind scheme and using the quasi-second-order TVD scheme with the symmetric limiter (SL.4) are presented in Figure 18(b). It should be observed that the surface pressure at the stagnation point is at least twice as large with the refined mesh. Further refinement indicates that this is a converged solution. The use of symmetric limiters, which are in general more diffusive, is justified for this application owing to the more stable convergence achieved when compared with the corresponding upwind limiters.

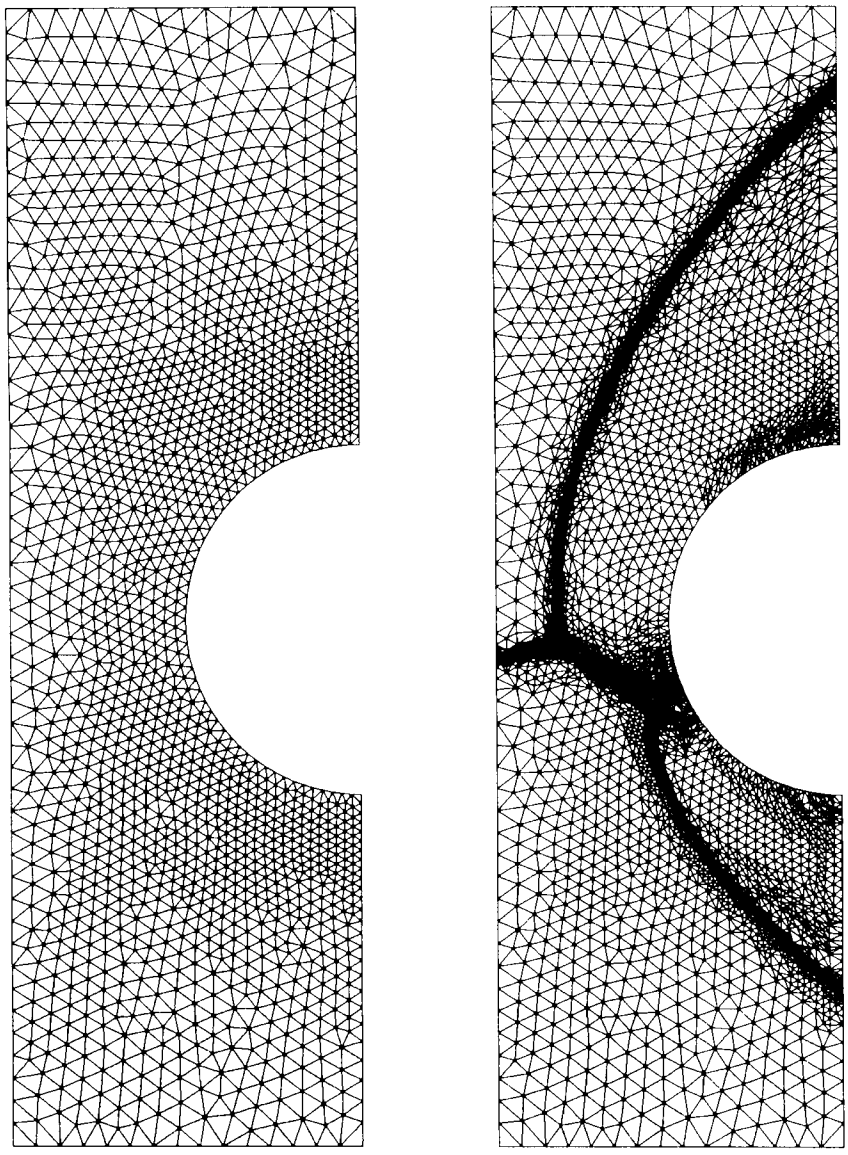

(a) (b)

Figure 16. Shock interaction on a circular cylinder at Mach 15: (a) initial mesh; (b) final adapted mesh

7. CONCLUSIONS

The Lax–Wendroff TVD scheme has been reviewed for the 1D Euler equations and the behaviour of the method with the use of some well known limiters with upwind or symmetric support has been examined. The choice of the limiter has been shown to be a crucial component of the overall performance of the algorithm, exerting a significant influence on the accuracy of the

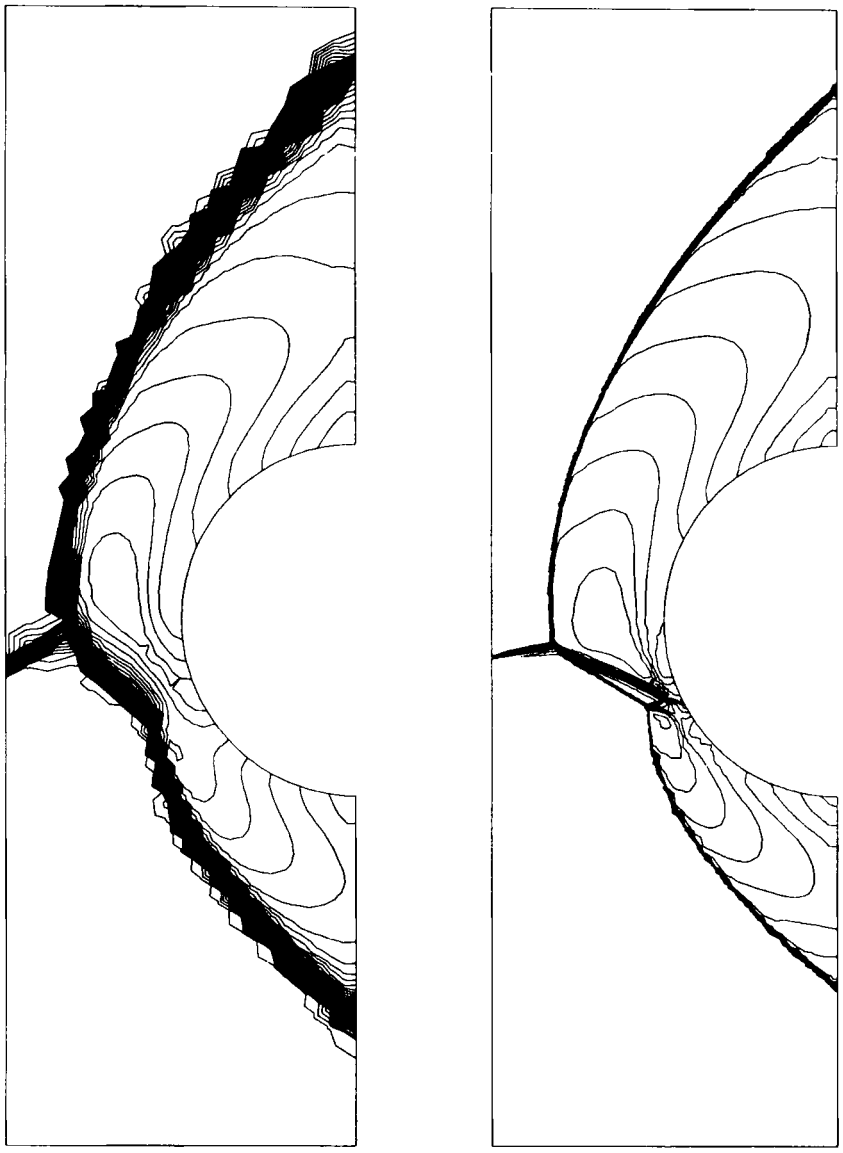

(a) (b)

Figure 17. Shock interaction on a circular cylinder at Mach 15: computed distribution of Mach number contours on (a) initial mesh and (b) final adapted mesh

numerical results, with the limiters computed on an upwind biased stencil leading to sharper resolution of discontinuities. Despite the better stability behaviour of the simulation and convergence rate in general achieved with the use of limiters computed on a symmetric support, they do not prevent failure of convergence towards machine zero in certain applications, and it was observed that the inclusion of a mechanism to freeze the limiters or the inclusion of a

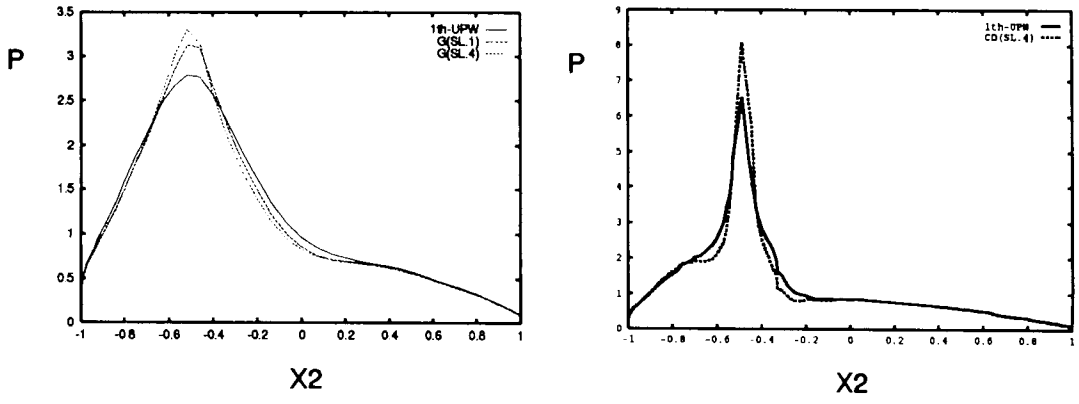

Figure 18. Shock interaction on a circular cylinder at Mach 15: computed distribution of pressure on cylinder surface on (a) initial mesh and (b) final adapted mesh

background diffusion can be necessary for good convergence behaviour, independently of the support used to compute the limiters. Further investigation in terms of accuracy, stability and convergence performance is required in order to analyse the effects of the inclusion of a background diffusion and in order to examine the combined effects of the limiter and the entropy correction adopted.

The production of a high-resolution algorithm for the solution of the compressible Euler equations on general unstructured triangular meshes has been described in a format which is directly extendable to 3D problems on tetrahedral meshes. The combination of a Galerkin finite element procedure with a rational way of supplying additional numerical dissipation by means of a TVD-limiting procedure proves to be successful in producing an accurate and robust algorithm. The flexibility for adapting the mesh and the inclusion of a mechanism to prevent the appearance of negative thermodynamic variables allow enhancement of the computed solution and prevent numerical instabilities in regions where the solution has very low values of pressure and density. The numerical results obtained, including some challenging supersonic and hypersonic applications, demonstrate the potential of the present scheme and encourage further effort to extend the approach to viscous flow simulations. Improvements in the computational efficiency can be considered by the inclusion of implicit time integration or multigrid acceleration techniques.

ACKNOWLEDGEMENTS

The first author would like to acknowledge the support received from CNPq (Brazilian Research Council). The other authors acknowledge the partial support provided by the Aerothermal Loads Branch of the NASA Langley Research Center under research grant NAGW 3290.

REFERENCES

1. T. J. Barth, 'Numerical aspects of computing viscous high Reynolds number flows on unstructured meshes', *AIAA Paper 91-0721*, 1991.
2. K. Morgan, J. Peraire and J. Peiró, 'Unstructured grid methods for compressible flows', *Rep.R-787 on Special Course on Unstructured Grid Methods for Advection Dominated Flows*, 1992, pp. 5.1–5.39.

3. J. Peraire, J. Peiró and K, Morgan, 'A 3-D finite element multigrid solver for the Euler equations', *AIAA Paper 92-0449*, 1992.
4. R. Löhner, K. Morgan, J. Peraire and M. Vahdati, 'Finite element flux-corrected transport (FEM-FCT) for the Euler and Navier–Stokes equations', *Int. J. Numer. Methods Fluids*, **7**, 1093–1109 (1987).
5. J. Peraire, K. Morgan, M. Vahdati and J. Peiró, 'The construction and behavior of some unstructured grid algorithms for compressible flows', *Proc. ICFD Conf. on Numerical Methods for Fluid Dynamics*, Oxford University Press, Oxford, 1994. (in press)
6. A. Harten, 'High resolution schemes for hyperbolic conservation laws', *J. Comput. Phys.*, **49**, 357–393 (1983).
7. H. C. Yee, 'Construction of explicit and implicit symmetric TVD schemes and their applications', *J. Comput. Phys.*, **68**, 151–179 (1987).
8. P. R. M. Lyra, K. Morgan, J. Peraire and J. Peiró, 'Unstructured grid FEM/TVD algorithm for systems of hyperbolic conservation laws', *Proc. 8th Int. Conf. on Numerical Methods in Laminar and Turbulent Flow*, Pineridge, Swansea, 1993, pp. 1408–1420.
9. M. T. Manzari, P. R. M. Lyra, K. Morgan and J. Peraire, 'An unstructured grid FEM/MUSCL algorithm for the compressible Euler equations', *Proc. VIII Int. Conf. on Finite Elements in Fluids: New Trends and Applications*, Pineridge, Swansea. 1993, pp. 379–388.
10. A. Jameson and W. Schmidt, 'Some recent developments in numerical methods for transonic flows' *Comput. Methods Appl. Mech. Eng.*, **51**, 467–493 (1985).
11. J. L. Thomas, 'An implicit multigrid scheme for hypersonic strong-interaction flowfields', *Proc. Fifth Copper Mountain Conf. on Multigrid Methods*, 1991.
12. S. F. Davis, 'TVD finite difference schemes and artificial viscosity', *ICASE Rep. 84–20*, 1984.
13. P. L. Roe, 'Generalised formulation of TVD Lax–Wendroff schemes', *ICASE Rep. 84–53*, 1984.
14. P. L. Roe, 'Approximate Riemann solvers, parameter vectors and difference schemes', *J. Comput. Phys.*, **43**, 357–372 (1981).
15. A. Harten, 'On a class of high resolution total-variation-stable finite-difference schemes,' *SIAM J. Numer. Anal.*, **21**, 1–23 (1984).
16. P. K. Sweby, 'High resolution schemes using flux limiters for hyperbolic conservation laws', *SIAM J. Numer. Anal.*, **21**, 995–1011 (1984).
17. H. C. Yee, 'A class of high-resolution explicit and implicit shock-capturing methods', *NASA Tech. Memo. 101088*, 1989.
18. P. Woodward and P. Colella, 'The numerical simulation of two-dimensional fluid flow with strong shocks', *J. Comput. Phys.*, **54**, 115–173 (1987).
19. G. D. Van Albada, B. Van Leer and W. W. Roberts, 'A comparative study of computational methods in cosmic gas dynamics', *Astron. Astrophys.* **108**, 78–84 (1982).
20. J. Peraire, M. Vahdati, K. Morgan and O. C. Zienkiewicz, 'Adaptive remeshing for compressible flow computations', *J. Comput. Phys.*, **72**, 449–466 (1987).
21. G. Sod, 'A survey of several finite difference methods for systems of nonlinear hyperbolic conservation laws', *J. Comput. Phys.*, **27**, 1–31 (1978).
22. V. Venkatakrishnan, 'Preconditioned conjugate gradient methods for the compressible Navier–Stokes equations', *AIAA J.* **29**, 1092–1100 (1991).
23. W. J. Rider, 'A comparison on TVD Lax–Wendroff methods', *Commun. Numer. Methods Eng.* **9**, 147–155 (1993).
24. J. N. Scott and Y. Y. Niu, 'Comparison of limiters in flux-split algorithms for Euler equations,' *AIAA Paper 93-0068*, 1993.